Separation of Ethanol and Water Using Graphene and Hexagonal Boron Nitride Slit Pores: A Molecular Dynamics Study

Anitha Kommu and Jayant K. Singh*

Department of Chemical Engineering, Indian Institute of Technology Kanpur, Kanpur-208016, India

S Supporting Information

ABSTRACT: The industries discharge a variety of pollutants, such as heavy metals, organic toxins, and oils, in water resources. Exposure of these contaminants in water causes adverse health effects on various forms of life. Novel materials are needed for the effective removal of pollutants from industrial wastewater. Graphene and hexagonal boron nitride (hBN) sheets are promising materials for removal of organic pollutants. In this work, the suitability of the sheets for the separation of the ethanol–water mixture is investigated by studying the adsorption and structural behavior of ethanol–water mixtures in slit pores with variable width (7–13 Å) using molecular dynamics simulations. The selectivity of ethanol is found to depend on the pore-width and nature of the pore walls. The selectivity of ethanol is highest for 9 Å pores and lowest for 7 Å pores, irrespective of the nature of the pore walls. However, selectivity of ethanol is relatively higher for hBN pores compared to the graphene pores, for all the considered pore widths. At a lower pore width, molecular sieving plays an important role for selective adsorption of ethanol molecules. On the other hand, at a higher pore width, selective adsorption of ethanol molecules is affected by the nature of the pore walls. The diffusion coefficients of water and ethanol molecules substantially decrease with a decrease in pore width for both graphene and hBN surfaces. The resident time of water and ethanol molecules decreases with increase in the slit-width. Furthermore, water and ethanol molecules confined in hBN pores show higher residence time and lower diffusion coefficient values compared to graphene pores. The adsorption behavior of water and ethanol molecules in the slit pores are analyzed using the potential mean forces, for water and ethanol molecules on the graphene and hBN surfaces, which are determined by umbrella sampling technique.
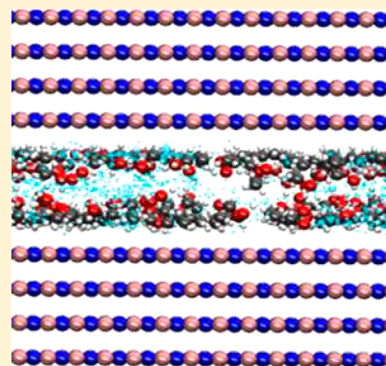
1. INTRODUCTION

The organic solvents and dyes discharged by the industries are primary pollutants of water resources. Thus, removal of such pollutants from contaminated water has become a subject of intense research.[1−3] Several techniques are proposed for the elimination of heavy metal ions and organic pollutants from wastewater, including ion-exchange,[4] coagulation and flocculation,[5] chemical precipitation,[6] reverse osmosis,[7] adsorption,[8] and other methods.[9,10] Among these techniques, the adsorption method is considered to be one of the simplest and most attractive methods for separating organic pollutants from wastewater. The ideal adsorbent material should exhibit high gravimetric capacity, easy separation from cleaned water and easy cleaning for long-term cycling. The most common adsorbents are activated carbon,[11] zeolites,[12] and natural fibers,[13] and other recent refined materials, including graphene capsules,[14] collagen nanocomposites,[15] polyurethane sponge,[16] polyurethane and iron oxide composites,[17] MnO$_2$ nanowires,[18] and graphene hydrogels.[19] These adsorbents have been used for removal of organic solvents such as alcohols, aromatic compounds, and dyes from aqueous phase.

The ethanol is one of the common organic pollutants in various industries, which cause adverse effects on environment and human health such as oxidative damage of brain, liver, stomach, and so on.[20,21] Therefore, it is necessary to separate

ethanol from aqueous solution efficiently. Numerous materials have been studied as potential membranes such as zeolites,[22,23] modified polydimethylsiloxane/polystyrene blended IPN pervaporation membranes[24] for the separation of ethanol–water mixtures.[25] Membranes based on zeolites such as NaA zeolites[23,26−29] show excellent performance for separation of water from ethanol compared to that based on polymers[30,31] and so on. However, these processes have significant disadvantages, which have low efficiency, unsatisfactory regeneration, and cycling ability. Thus, development of new and advanced materials is necessary to overcome these principal drawbacks. In this direction, two-dimensional materials (e.g., graphene and hexagonal boron nitride) have attracted much recent attention due to their unique properties and high-surface area.[32,33] In recent years, the most prominent member of the family of layered materials has been graphene, which serves as a building block for few-layered graphene and graphite as well as for single and multiwalled carbon nanotubes.[34] The inorganic analog of graphene, sometimes referred to as "white graphene"[35−37] is hexagonal boron nitride (hBN).[38−40] Experiments are performed to study the adsorption behavior of

Table 1. Summary of the Nonbonded and Bonded Interactions of Water and Ethanol Molecules[a]

molecule	site	charge (e)	σ (Å)	ε (kcal mol^{-1})
water	O	−0.8476	3.166	0.15525
	H	0.4238	0.000	0.0000
ethanol	C1	−0.1800	3.500	0.066
	C2	0.1450	3.500	0.066
	O(C=O)	−0.6830	3.120	0.170
	H1	0.0600	2.500	0.030
	H2	0.0600	2.500	0.030
	HO(O−H)	0.4180	0.000	0.000
graphene	C	0.000	3.400	0.05566
hBN	B	0.930	3.453	0.09487
	N	−0.930	3.365	0.14477

molecule	bond stretching	k_r (kcal mol^{-1} Å^{-2})		r_{eq} (Å)
water	O−H			1.000
ethanol	C−C	536		1.529
	C−H	680		1.090
	C−O	640		1.410
	O−H	1106		0.945

molecule	angle stretching	k_θ (kcal mol^{-1} rad^{-2})		θ_{eq} (deg)
water	H−O−H			109.47
ethanol	H−C−C	75		110.7
	C−C−O	100		109.5
	H−C−H	66		107.8
	H−C−O	70		109.5
	C−O−H	70		109.5

molecule	dihedral	V_1 (kcal mol^{-1})	V_2 (kcal mol^{-1})	V_3 (kcal mol^{-1})
ethanol	H−C−C−O	0.0	0.0	0.468
	H−C−C−H	0.0	0.0	0.318
	C−C−O−H	0.356	0.174	0.492
	H−C−O−H	0.0	0.0	0.450

[a]In the case of ethanol, C1 and C2 stand for the carbon atom of −CH$_3$ and −CH$_2$ group. H1, H2, and OH are the hydrogen atoms of −CH$_3$ and −CH$_2$, and −OH group, respectively.

ethanol−water within slit pores, composed of graphene layers.[41] The hydrophobic nature of graphene surface induces preferential ethanol adsorption within the slit pore. Recently, some experimental studies have demonstrated that the boron nitride exhibits higher adsorption of organic pollutants than those of the adsorbents reported previously.[42−44]

However, most of the studies on the ethanol−water mixture have focused on the performances of the adsorbents, especially in terms of the adsorbed number of molecules, without much of molecular insight into the separation behavior.[42,43] In contrast, few works based on molecular dynamics simulations have focused on the properties of alcohol−water mixtures confined in nanopores. For example, molecular simulations studies have shown the competitive binding/adsorption between alcohols and water inside single-walled carbon nanotubes (SWCNT) bundle.[45] Yang et al.[26] employed Monte Carlo and molecular dynamics techniques to study the preferential adsorption and diffusion of ethanol−water system on silicate crystal. The structural and physiochemical behavior of alcohol−water mixture are different from that of pure components due to its hydrogen bonding effect.[46−48] Several studies demonstrated that ethanol−water mixture could undergo phase separation under hydrophilic nanopores.[49−51] Zhao et al.[52] studied the effect of pore width and composition of ethanol−water mixtures confined within slit-shaped graphene nanopores. Phan et al.[49] have investigated the sorption, structure, and dynamics of the ethanol−water mixtures confined in alumina pores. Recently, some experiments[42−44] investigated that the

hBN exhibits higher adsorption of ethanol compared to other adsorbents. However, fundamental insights into the adsorption of ethanol−water mixtures within the slit-shaped pore of hBN surface are not well understood. Furthermore, how the adsorption behavior of ethanol−water mixtures is different from that of graphene-based slit pores is not known. To this end, we employed MD simulations to investigate the selectivity of ethanol−water in slit-shaped graphene and hBN pores. We report details concerning structural (i.e., density profiles, hydrogen bonding, and molecular orientation) and dynamical properties (i.e., self-diffusion coefficients and residence time) of ethanol−water confined in slit pores. In order to compare the properties of confined water and ethanol molecules using two different materials (graphene and hBN), we have considered three pore sizes (7, 9, and 13 Å) under identical conditions. The rest of the article is organized as follows. In Section 2 we describe the models and methodology used in this work. Section 3 presents the results and discussions, followed by the conclusion in Section 4.

2. MODELS AND METHODS

In this work, the all-atom optimized potentials for liquid simulations force-field (OPLS-AA)[53] is used to describe the graphene and hBN pores[54,55] and ethanol[56] molecules. SPC/E[57] water model is used for water−water interactions. Nonbonded interactions between the graphene and hBN surface with ethanol−water system are described by eq 1. The bond stretching and bending potentials are described by
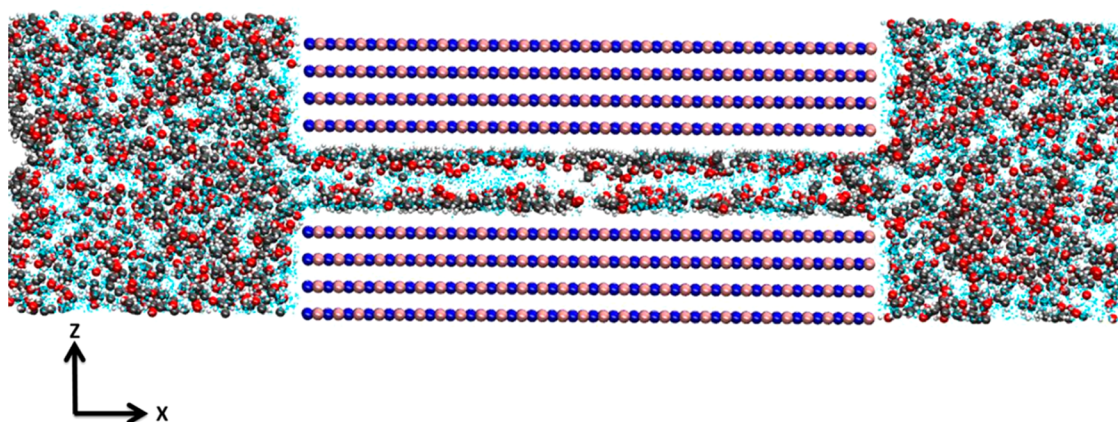
Figure 1. Representative simulation snapshot for the water/ethanol mixture in contact with the 13 Å hBN pore. Red and white spheres represent oxygen and hydrogen atoms and gray spheres represent carbon atoms of ethanol molecules, respectively. Cyan color represents water molecules. Pink and blue spheres represent the boron and nitrogen atoms of hBN surface, respectively.

harmonic potentials, as in eq 2. The torsion interactions are calculated using OPLS-AA force field (eq 3).

$$U_{nonbonded} = 4\varepsilon_{ij}\left[\left(\frac{\sigma_{ij}}{r}\right)^{12} - \left(\frac{\sigma_{ij}}{r}\right)^{6}\right] + \frac{q_i q_j}{4\pi\varepsilon_0 r_{ij}} \tag{1}$$

$$U_{stretching} = \frac{1}{2}k_b(r - r_0)^2; \quad U_{bending} = \frac{1}{2}k_\theta(\theta - \theta_0)^2 \tag{2}$$

$$U_{torsion} = \frac{1}{2}V_1[1 + \cos(\phi)] + \frac{1}{2}V_2[1 - \cos(2\phi)]$$
$$+ \frac{1}{2}V_3[1 + \cos(3\phi)] + \frac{1}{2}V_4[1 - \cos(4\phi)] \tag{3}$$

where σ and ε, the nonbonded parameters, are the Lennard-Jones diameter and energy well depth, respectively. q is the partial atomic charges, r_{ij} is the atomic separation between atoms i, j, and ε_0 is the dielectric permittivity constant. k_b and k_θ are bond and angle force constants, respectively. The r and r_0 are instantaneous and equilibrium bond length values, and θ and θ_0 are the instantaneous and equilibrium bending angles, respectively. V_1, V_2, V_3, and V_4 are the Fourier coefficients and ϕ is the dihedral angle, respectively. Table 1 summarizes the nonbonded and bonded interactions used in this work. The Lennard-Jones parameters for unlike interactions are calculated using Lorentz−Berthelot mixing rules.

The residence time of water and ethanol molecules inside the slit pores is calculated using residence auto correlation function $C_R(t)$:

$$C_R(t) = \frac{\langle \sum_{i=1}^{N} \theta_i(t_0 \theta i)(t + t_0) \rangle}{\langle \sum_{i=1}^{N} \theta_i(t_0)\theta_i(t_0) \rangle} \tag{4}$$

$$C_R(t) = A \exp[-(t/\tau_s)] \tag{5}$$

where $\theta_i(0) = 1$ when the molecule i is found inside the pore at time $t = 0$. If an appended molecule continuously remains inside the pore as the time "t" progresses, then $\theta_i(t) = 1$; $\theta_i(t) = 0$ when the molecule exits the pore. The $\theta_i(t)$ remains equal to 0, even if the molecule eventually returns inside the pore. The residence time (τ_s) is evaluated by fitting an exponential form, as shown in eq 5, to the $C_R(t)$ values.

Following the approach of Liu et al.,[58] the translational molecular movement parallel to the surface (in-plane parallel

diffusion coefficients, D_{xy}) is calculated from the mean-square displacement of the molecules, parallel to the surface using eqs 6 and 7.

$$MSD_{xy}(t) = \frac{1}{N}\langle \sum_{i=1}^{N} [x_i(t) - x_i(t_0)]^2 + [y_i(t) - y_i(t_0)]^2 \rangle \tag{6}$$

where $([x_i(t) - x_i(t_0)]^2 + [y_i(t) - y_i(t_0)]^2)$ is the mean square displacement along the plane of the pore and N is the number of atoms. The linear slope of the curve during the time interval $t = 0-300$ ps is calculated to determine D_{xy} via the Einstein equation.

$$D_{xy} = \frac{1}{4}\lim_{t\to\infty}\frac{d}{dt}(MSD_{xy}) \tag{7}$$

In order to determine the selectivity of ethanol adsorption, we use the following expression,[59]

$$s = \left(\frac{y_A^a}{y_B^a}\right)\left(\frac{x_{bulkB}}{x_{bulkA}}\right) \tag{8}$$

where y_A^a and y_B^a are the mole fractions of components A and B, in the adsorbed phase (inside the pore), and x_{bulkA} and x_{bulkB} are the mole fractions of components A and B in the bulk phase.

Hydrogen bonds (HBs) between any two water molecules are determined by the fulfillment of the following three conditions:[60,61] $R_{OO} < 3.5$ Å, $R_{OH} < 2.45$ Å, and HO---O angle $<30°$. The HB between any two ethanol molecules[62] (i.e., ethanol−ethanol, ethanol−water, and water−ethanol) exists if the following three conditions are satisfied: $R_{OO} < 3.5$ Å, $R_{OH} < 2.60$ Å, and HO---O angle $<30°$. The average number of HBs per ethanol molecule is defined by the ratio of the total number of ethanol−ethanol and ethanol−water HBs formed to the total number of ethanol molecules.

We conducted MD simulations for ethanol molecules dissolved in explicit water. Figure 1 presents a schematic picture of the simulation box containing slit pore made up of hBN (or graphene) surfaces (walls). Three different pore widths (H), 7, 9, and 13 Å, are considered for both the materials. Pore width of the slit-pore is taken as the distance from the center of the atoms of the top layer of the bottom wall to the atoms of the bottom layer of the top wall. The interlayer
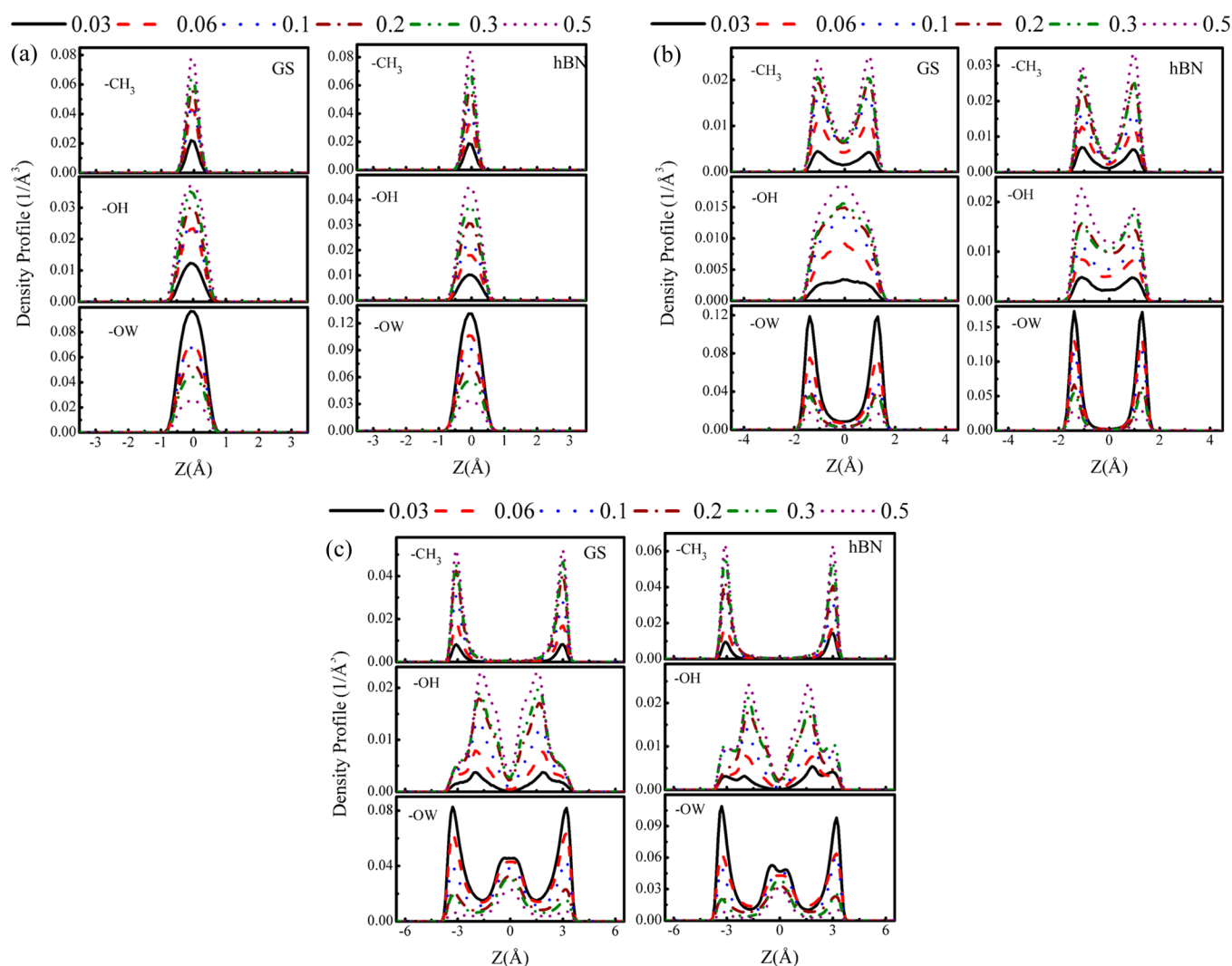
Figure 2. (a) Density profiles of oxygen atom in water, methyl and hydroxyl groups in ethanol molecule in the 7 Å graphene (GS) and hBN slit-shaped pores with varying mole fraction of ethanol. (b) Density profiles of oxygen atom in water, methyl and hydroxyl groups in ethanol molecule in the 9 Å graphene (GS) and hBN slit-shaped pores with varying mole fraction of ethanol. (c) Density profiles of oxygen atom in water, methyl and hydroxyl groups in ethanol molecule in the 13 Å graphene (GS) and hBN slit-shaped pores with varying mole fraction of ethanol.

distances between graphene and hBN sheets are separated by 3.35 and 3.33 Å respectively. The simulation box is periodic in the x, y, and z directions. The dimensions of simulation box for graphene and hBN slit pores along the x and z directions are 400 and 36.31 Å and 400 and 36.34 Å, respectively. The size of the simulation box is larger in the x direction to ensure that the bulk phase is far from the solid surface. Furthermore, to maintain the pressure in the liquid system at near ambient conditions, we allow the formation of a vacuum of 200 Å width along the x direction. Simulations are carried out for five different mole fractions of ethanol (0.03, 0.06, 0.1, 0.2, 0.3, and 0.5). The total number of molecules (water + ethanol) is constant for all systems. All simulations are performed in the NVT ensemble using the LAMMPS[63] molecular dynamics package. Particle−particle particle−mesh (PPPM)[64] technique is applied for the calculation of long-range electrostatic forces. The cutoff for LJ interactions is set to be 10 Å. The SHAKE algorithm[65] is used to fix the bond length and angle for water molecules. The bond length and angles of ethanol molecules are unrestrained in the MD simulations. All simulations are performed at a temperature of 300 K. At the start of the

simulation, both sides of the slit pore having two reservoirs with the same mole fraction of ethanol molecules. The total simulation time is 30 ns for each system, with an integration time step of 1 fs. Data analysis is conducted over the last 10 ns of the simulations. A Nosé−Hoover thermostat[66] is used to maintain the system temperature with a relaxation constant of 1.0 ps.

3. RESULTS AND DISCUSSION

3.1. Structural Properties of the Confined Ethanol−Water Systems. Figure 2 presents the atomic density profile of oxygen atom (OW) of water molecules within the graphene and hBN pores, of slit widths 7, 9, and 13 Å, for varying mole fraction of ethanol. In the figure, $z = 0$ corresponds to the center of the pore. The number of density layers of water molecules increases with an increase in pore width. The density profile of oxygen atom, within the 7 Å pore width, shows one peak at the center of the pore, for both hBN and graphene pores (surfaces), as shown in Figure 2a. The pore size is not enough to accommodate more than one layer of water molecules, and the water molecules are localized at the center
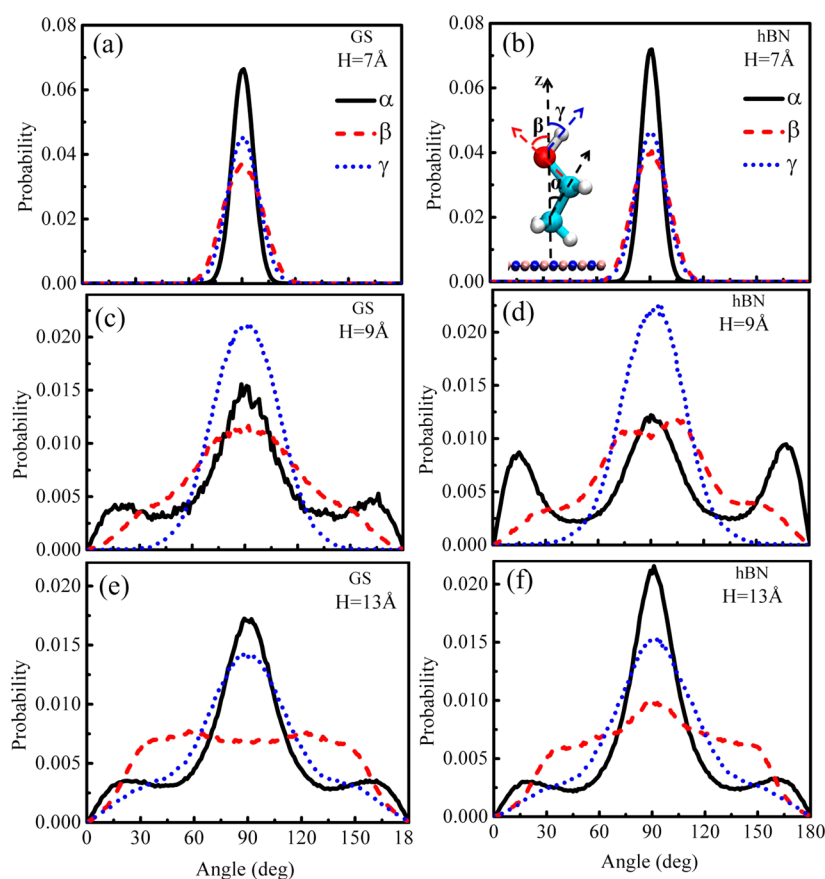
Figure 3. Normalized orientation angle (α, β, γ) distributions of confined ethanol molecules within the 7, 9, and 13 Å graphene (GS) and hBN slit-shaped pores for 0.3 M ethanol−water mixture.

of the pore (7 Å). Simulation snapshots of confined water molecules shown in Figure S1a,b in the Supporting Information provide the visual evidence of the formation of single layer of water molecules at the center of the pore. On the other hand, the density profile of confined water molecules in 9 Å pore shows two distinct peaks, as shown in Figure 2b. With an increase in the pore size to 13 Å, the number of density layers increases as reflected by three distinct density peaks, as shown in Figure 2c. As expected, our results show that the number of layers increases with an increase in slit pore size. These results are consistent with simulation results reported for pure water confined in graphene slits.[67,68] The density distribution of confined water molecules shows two distinct peaks that are localized near the pore surface, while the third peak is located at the center of the pore. In general, the density distributions of oxygen atoms (OW) of water molecules within the 9 and 13 Å pores are similar for both hBN and graphene pores. The snapshot of confined water molecules, shown in Figure S1, parts c−f in the Supporting Information, supports the observation. Interestingly, the intensity of density profile of water molecules within the hBN pores, irrespective of the pore width, is more pronounced compared to that in the graphene pores. This is due to stronger interactions between hBN and water molecules compared to that of graphene, which is also observed in an earlier work where contact angle of water on graphene surface was found to be higher than that on hBN surface.[55] The ethanol content also affects the adsorption amount of water. This is evident from the decrease in the peak height of water density profiles with increase in the ethanol mole fraction. This indicates that the number of water

molecules confined within the pore decreases with increase in ethanol concentration.

Figure 2 also presents the density profiles for methyl ($-CH_3$) and hydroxyl ($-OH$) groups of ethanol molecules in all pores with varying mole fraction of ethanol. In the pore size 7 Å, the methyl and hydroxyl groups are concentrated within the center of the pore for both graphene and hBN pores (Figure 2a). The snapshots of confined methyl and hydroxyl groups of ethanol molecules shown in Figures S2 and S3, parts a and b, in the Supporting Information, illustrate the single layer of ethanol molecules at the center of the 7 Å pore. In the case of wider pores (9 and 13 Å), the methyl group of ethanol molecules shows well-defined density layers near the solid surfaces. The peaks of the methyl group density profile are closer to the pore walls than that of the hydroxyl group density profiles due to its relatively more affinity toward the pore walls. However, polar hydroxyl groups are located outward from the pore walls to maintain a hydrogen bond with the adjacent solvent layer. This also reflected in the simulation snapshots where the confined ethanol molecules clearly exhibit two layers of methyl group of ethanol molecules within 9 and 13 Å, as shown in Figure S2, parts c−f, in the Supporting Information. Moreover, the hydroxyl group of ethanol molecules accumulate near the pore center for all pores considered in Figure S3, parts c−f, respectively, in the Supporting Information. The hydroxyl groups of ethanol molecule is more widely distributed at the center of 9 Å graphene pore, while they form two layers (though not well pronounced) within hBN pore of the same width, which is in line with the density profiles. The height of methyl ($-CH_3$) and hydroxyl ($-OH$) groups density profile
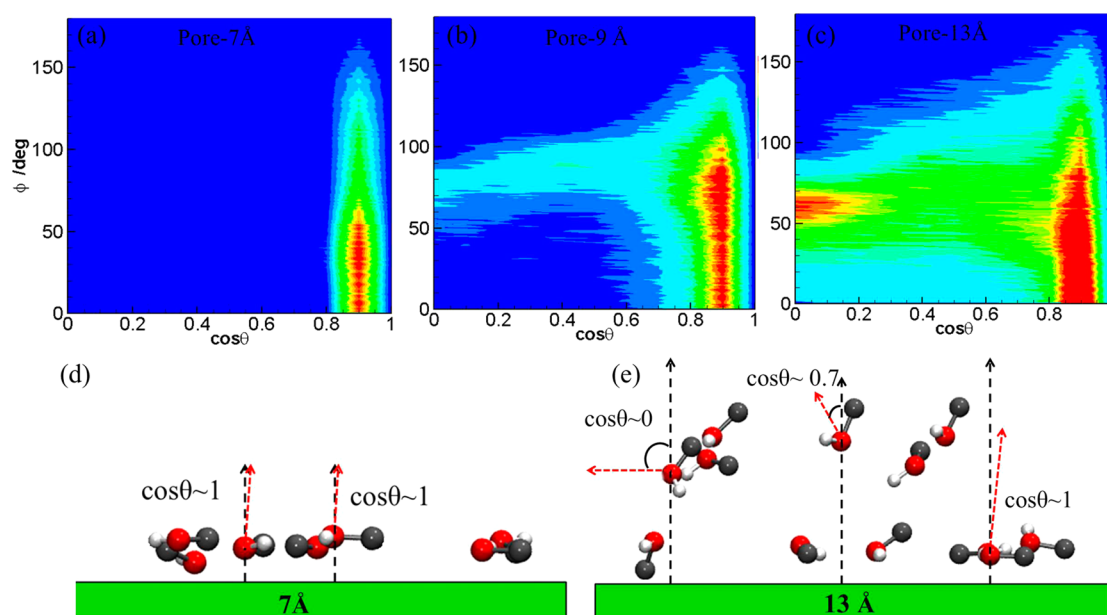
Figure 4. Bivariate joint distribution of the angles θ and ϕ of ethanol molecules for 0.3 M ethanol−water mixture: (a) pore 7 Å, (b) pore 9 Å, and (c) pore 13 Å. Dark shades of red indicates higher probabilities and blue shades indicates zero probabilities. (d, e) Snapshots of ethanol molecules within different pores 7 and 13 Å. Gray, red, and white color represents carbon, oxygen, and hydrogen atoms, and green color represents the surface.

inside the slit pores 7, 9, and 13 Å for both surfaces (graphene and hBN) increases with increasing ethanol content. This is primarily due to the increased number of ethanol molecules within the pore with increasing ethanol mole fraction. In all the three pores (7, 9, and 13 Å) the density profiles of methyl and hydroxyl groups of ethanol molecule in contact with the hBN surface are relatively pronounced compared to the graphene surface. This indicates stronger propensity of ethanol to adsorb on the hBN surface. To elucidate the behavior of ethanol molecules inside the slit pores of 7, 9, and 13 Å, we next present the orientation distribution and hydrogen bond of ethanol molecules within the graphene and hBN slit pores.

3.2. Orientation Distribution and Hydrogen Bond of Confined Ethanol Molecules. In order to characterize the configuration of ethanol, we define α, β, and γ as the orientation angles between the z-axis and $CH_3−CH_2$, $CH_2−OH$, and O−H bonds of ethanol, respectively. Figure 3 presents the normalized orientation angle distribution of confined ethanol molecules inside the three slit pores (7, 9, and 13 Å) for 0.3 M ethanol−water mixture. The confined environment significantly affects the orientation distribution of ethanol molecules within the slit pores. In the 7 Å pore, all three angles show a single peak at 90° (see Figure 3a,b). This indicates that the $CH_3−CH_2$, $CH_2−OH$, and O−H bonds prefer to align along the graphene and hBN walls. With an increase in the pore sizes (9 and 13 Å), a remarkable change is observed in the orientation distribution of ethanol molecules. For 9 and 13 Å pore sizes, the orientation angle α has a broad distribution with three major peaks at 20°, 90°, and 160°, irrespective of the nature of the pore walls (see Figure 3c−f). The orientation distribution of the $CH_3−CH_2$ bond is relatively more pronounced at 90° for both surfaces, indicating that the $CH_3−CH_2$ bonds are likely to stay along the z-axis. The orientation distribution of $CH_3−CH_2$ bond is further accentuated with an increase in the pore size, as seen for 13 Å slit pore. It is noted that the intensity of peaks at 20° and 160° is higher for hBN compared to the graphene wall, in 9 Å

pore. For 9 Å, the corresponding orientation distribution angle β displays a broad peak at 90° for graphene pore (see Figure 3c). On the other hand, it shows two distinct peaks at 75° and 107° for hBN pore (see Figure 3d). In the case of 13 Å, the corresponding orientation distribution angle β displays peaks at 60° and 130° for graphene pore, though not relatively sharp (see Figure 3e). On the other hand, the corresponding distribution for hBN pore shows sharper peak at 90°. It is noted that β distribution shows presence of angles 30° and 150° in the form of shoulder in hBN pore, which is more prominent in 13 Å pore compared to 9 Å pore (see Figure 3f). These results are in line with the density profiles of ethanol as shown in Figure 2. The behavior of β distribution is mainly governed by the formation of hydrogen bond between neighboring ethanol molecules within the pore, which affects the position of oxygen atom resulting in the deviation of ethanol molecule from the axial plane of the pore. The orientation angle (γ) within the 7, 9, and 13 Å pores (Figure 3c−f) shows that the orientation distribution of O−H bond exhibits a strong peak at 90° for both the pore walls (hBN and graphene). This indicates that the O−H bonds are parallel to the hBN and graphene surfaces. However, the probability distribution of O−H bond is relatively broader at larger pore width, 13 Å(see Figure 3e,f). This implies that the nature of the pore, that is, hBN or graphene, have no obvious impact on the orientation angle γ distribution.

The orientation of the molecules relative to a flat surface can be described unambiguously by the bivariate joint distribution of two independent orientational parameters.[69−71] The angular polar coordinates θ and ϕ of the surface normal vector in a Cartesian frame fixed to the individual molecules is a good choice for the orientational parameters. Here the angle θ is formed by the two spatial vectors, that is, the z-axis of the local frame and the surface normal vector **X**, whereas ϕ is defined as angle formed by two vectors (i.e., the projection of **X** to the xy plane of the local frame and the x-axis of the local frame) that are restricted to lie in the xy plane of the local frame. In the case
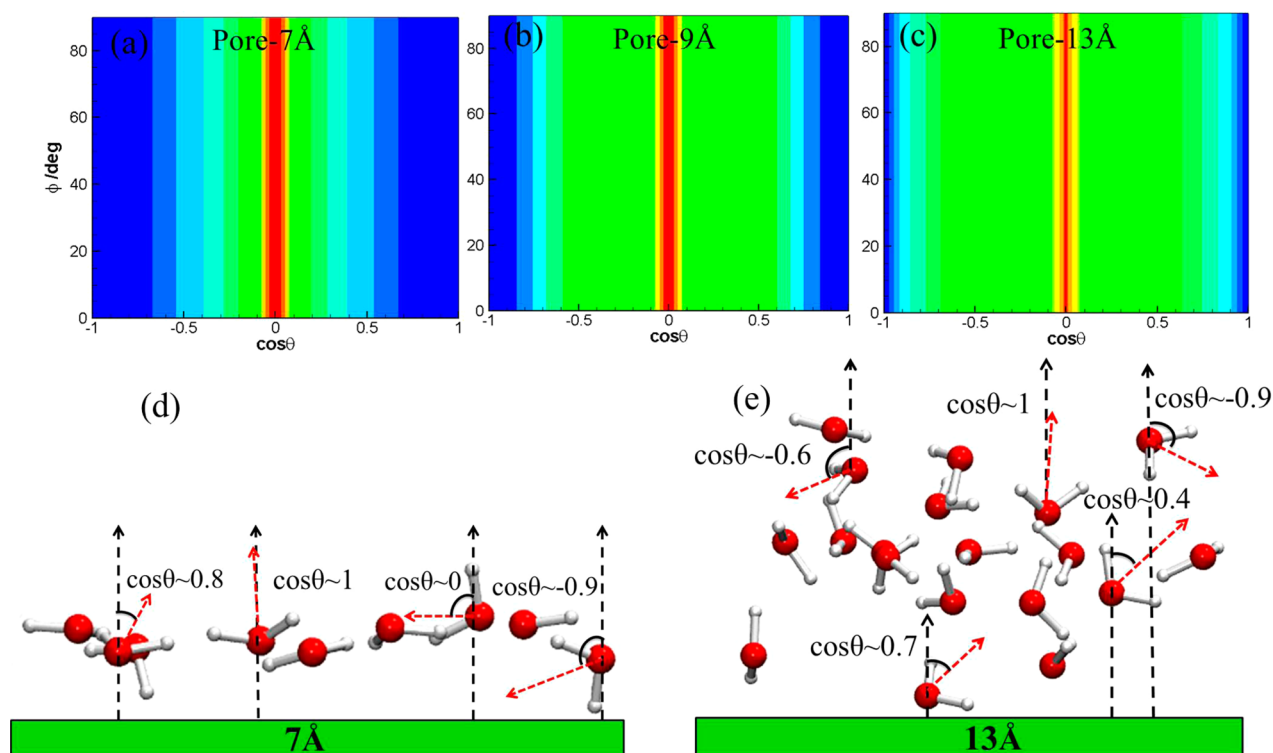
Figure 5. Bivariate joint distribution of the angles θ and ϕ of water molecules for 0.3 M ethanol−water mixture: (a) pore 7 Å, (b) pore 9 Å, and (c) pore 13 Å. Dark shades of red indicate higher probabilities and blue shades indicate zero probabilities. (d, e) Snapshot of ethanol molecules within different pores 7 and 13 Å. Red and white colors represent oxygen and hydrogen atoms and green color represents the surface.

of ethanol molecules, the x-axis of the local frame lies along the CH$_2$−O bond of ethanol molecule, z-axis is molecular normal vector, and the y-axis is perpendicular to the previous two, with the x-coordinate of the H atom being positive and its y-coordinate is negative (given that the origin of the frame is the O atom in both cases). Because of this definition, these local frames are chosen in such a way that, in the case of ethanol, the angle θ falls in the range of 0−90° ($0 \leq \cos \theta \leq 1$), whereas the angle ϕ can take value between 0° and 360°. In the case of water molecules, the local Cartesian frame is defined as x-, y-, and z-axes, which coincide with the normal vector, H−H vector, and dipole vector, respectively. Due to the symmetry of the molecules, these local frames are always chosen in such way that angle ϕ for water molecules lies in the range of $0° \leq \phi \leq 90°$.

The resulting bivariate distributions, $P(\cos \theta, \phi)$, of ethanol molecules are plotted in Figure 4, as obtained in the three different slit pores. In the case of ethanol confined within 7 Å pore, the maximum of the $P(\cos \theta, \phi)$ distribution peak is around $\cos \theta = 0.95$ and $\phi = 50°$, respectively. The peak corresponds to the preferred orientation of ethanol molecules. In this orientation, the ethanol molecules remain parallel to the surface within 7 Å pore. It is also evident from the snapshot (Figure 4d) that the ethanol molecules prefer to be in a single-file structure along the surfaces. Increasing the pore widths to 9 and 13 Å of the system leads to sudden changes in the preferred orientations of the confined ethanol molecules. The peak orientation of ethanol molecules is shifted to smaller $\cos \theta$ values and becomes broader along the ϕ axis, as shown in Figure 4b,c. The broadening of the peak is observed in the larger pore width that is attributed to the increase in number of ethanol and water molecules within the pores, which affects the orientation of ethanol molecules. Figure 4e presents the

corresponding snapshots for illustration, where it is evident that the ethanol molecules prefer to stand on the surface. The polar groups of ethanol molecules point toward the pore center, which has been reported in previous studies.[72] This indicates that the confinement effect decreases with an increase in pore width. We can conclude that the configuration of ethanol molecules transforms from parallel state to the standing state with increase in the pore size.

The bivariate distributions of the water molecules are shown in Figure 5. The preferred orientation of water molecules changes with pore size. Within 7 Å pore the maximum peak of the distribution is at around $\cos \theta = 0$ and $\phi = 90°$, which is the preferred orientation of water molecules. Furthermore, it is evident from the snapshots shown in Figure 5d that the water molecules prefer to align along the surfaces (corresponding to $\cos \theta = 0$). In the case of 9 and 13 Å pores, more water molecules move inside the larger pores, and due to the large space, different orientations of water molecules are probably leading to broadening of the angle distribution. This is also evident from the snapshot (Figure 5e) that the water molecules show other preferred orientations within larger pore widths.

To explore the variation of ordering of ethanol molecules, we have calculated the average number of hydrogen bonds per ethanol molecule (HB) inside the pore size. Figure 6 shows the average number of hydrogen bond (HB) per ethanol molecule within the slit pore as a function of pore widths (7, 9, and 13 Å) for 0.3 mole fraction of ethanol. For pore size 7 Å, the number of HB per ethanol molecules is higher for the graphene pore. In the case of 9 Å pore, HB per ethanol molecule is higher for both types of pores (graphene and hBN) compared to the 7 and 13 Å pores. The HB number between ethanol molecules increases due to the decrease of water consumption inside the slit pore. This is in line with the density profiles of water and
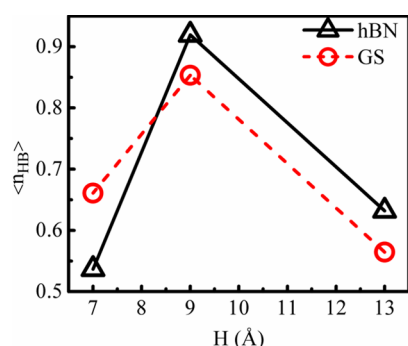
Figure 6. Average number of HBs per ethanol molecule within the pore as a function of pore size for 0.3 M ethanol−water mixture. The error bars are smaller than the symbols.

ethanol molecules inside the slit pore 9 Å. Thus, the ethanol molecules have higher probability to form the ethanol−ethanol hydrogen bonds per ethanol molecule within slit pore 9 Å compared to 7 and 13 Å slit pores. The number of HBs per ethanol molecule decreases in the wider 13 Å pores, which implies that the ethanol−ethanol HB structure gets broken with increase in water consumption inside the pore.

The stability of HBs between ethanol molecules within the pores can be characterized in terms of time correlation function. The intermittent time correlation function $C_{HB}(t)$ of hydrogen bonds within the pores is quantified as

$$C_{HB}(t) = \frac{\langle h(0)h(t) \rangle}{\langle h(0)h(0) \rangle} \qquad (9)$$

$$C_{HB}(t) = A \exp[-(t/\tau_s)] \qquad (10)$$

where $h(0)$ is unity when the corresponding HBs pair is found inside the pore at time $t = 0$. If a tagged HB pair continuously remains in the pore as time t, then $h(t)$ equals to unity and is zero otherwise. It is possible to estimate how long the HBs exists between ethanol−ethanol molecules within the slit pores by studying the intermittent time correlation function $C_{HB}(t)$. The faster the $C_{HB}(t)$ decays to zero, the shorter is the time ethanol molecules remained hydrogen bonded with other ethanol molecules. Figure 7 shows that the $C_{HB}(t)$ decay rate
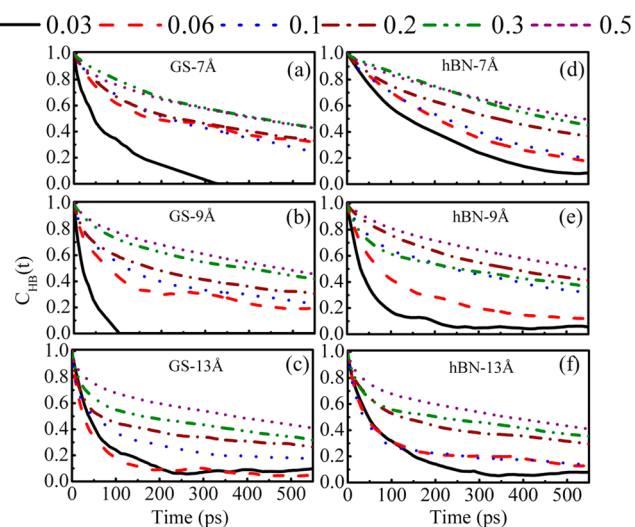
Figure 7. Intermittent time correlation function $C_{HB}(t)$ of ethanol molecules inside the pores.

for ethanol−ethanol increases with increasing mole fraction of ethanol. Within the first 500 ps, the analysis suggests that the $C_{HB}(t)$ obtained for ethanol molecules decays faster in the order of 0.03 > 0.06 > 0.1 > 0.2 > 0.3 > 0.5 ethanol mole fraction, within three different slit pores. Regarding the ethanol−ethanol $C_{HB}(t)$ decay rate decreasing with increases in water content, this is due to fewer ethanol molecules available to form HBs. In the 7 Å pore, the decay rate of time correlation function is the slowest because of enhanced HB interaction caused by the organized structure of ethanol molecule within the pore (shown in Figure S2 in the Supporting Information), which is also reported in previous studies.[72−74] In the case of 9 Å pore, the decay rate of time correlation function is the slower compared to other two pores for all mole fraction of ethanol. These results confirm that the ethanol−ethanol HBs exists for a longer time within 9 Å pore. However, for the wider pores 13 Å the decay rate of time correlation function is faster compared to the narrow pore 7 Å for all mole fractions. This indicates that the HBs between ethanol−ethanol molecules do not remain for larger time in the 13 Å pore. It implies that relatively larger number of water molecules in 13 Å pore gradually breaks ethanol−ethanol HB structures. The results of $C_{HB}(t)$ also confirm the stronger HB behavior of ethanol molecules in 9 Å pore compared to 7 and 13 Å pores. Therefore, the selectivity of ethanol molecules within 9 Å pore is higher compared to other pore sizes.

We also evaluated the residence time (τ_s) of HB between ethanol molecules using intermittent time correlation function $C_{HB}(t)$ using eq 10. The lower decay rate of $C_{HB}(t)$ indicates a higher residence time of HB formed between ethanol molecules inside the pore. Figure 8 presents the residence time of HBs
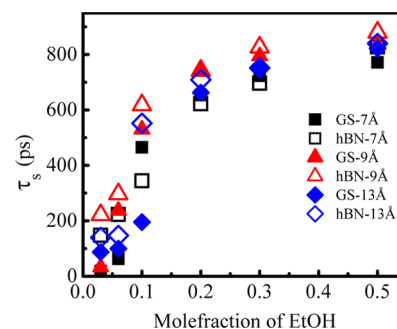
Figure 8. Residence time of HBs between ethanol molecules within the three slit-shaped pores as a function of ethanol mole fraction. Filled symbols are for hBN pores, and open symbols are for GS pores.

between ethanol molecules within different slit pores (7, 9, and 13 Å) using both graphene and hBN surfaces. The residence time of HBs between ethanol molecules increases with increase in the mole fraction of ethanol. This implies that the formation of HB between ethanol molecules inside the pore increases with increasing mole fraction of ethanol in the mixture. Interestingly, we find that the confined ethanol molecules have higher residence time of HBs between ethanol molecules within the pore 9 Å compared to the other pore sizes (7 and 13 Å). This further corroborates our observation on the selectivity of ethanol molecules within 9 Å pore, which is significantly higher compared to 7 and 13 Å pores.

3.3. Dynamical Properties of Confined Ethanol/Water Mixtures. In order to evaluate the mobility of the ethanol−water system inside the graphene and hBN slit-shaped pore, the

molecular diffusion coefficients of water and ethanol molecules are calculated. We have studied the in-plane diffusion coefficients of the confined ethanol and water molecules from the mean square displacement (using eqs 5 and 6). Figure 9a,b
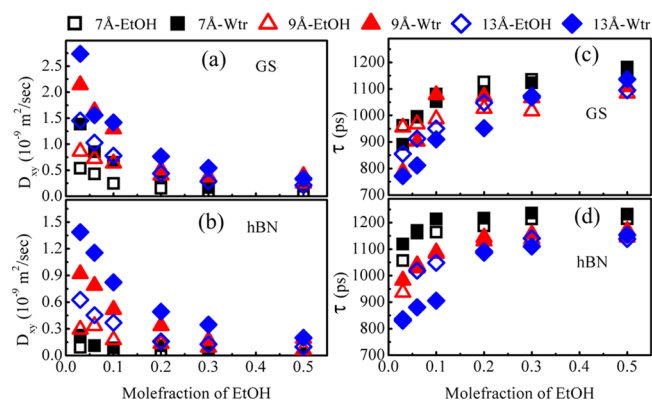
Figure 9. Diffusion coefficient for water and ethanol molecules within three slit-shaped pores as a function of ethanol mole fraction: (a) graphene (GS), (b) hBN surface. Residence time for water and ethanol molecules within three slit-shaped pores as a function of ethanol mole fraction: (c) graphene (GS), (d) hBN surface. Filled symbols are for water molecules, and open symbols are for ethanol molecules.

presents the in-plane diffusion coefficient of ethanol molecules as a function of its mole fraction in graphene and hBN pores. The larger the value of diffusion coefficient, the faster the molecules diffuse inside the slit pore. As the slit width is increased from 7 to 9 Å, the mobility of water molecules shows a slight increase that is indicated by the increase in the diffusion coefficient. This is particularly more evident at lower ethanol mole fractions. At 7 Å pore, we have found lower diffusion coefficient of ethanol and water molecules for both hBN and graphene pores. The diffusion behavior of water confined inside the narrow slit pore 7 Å of graphene and hBN pores is akin to that seen for water inside carbon nanotubes (6,6).[75,76] Further increases in the pore size 9 Å, the diffusion coefficient increases for both the molecules. Within the pore 9 Å, water and ethanol molecules display the higher mobility in the graphene pore compared to the hBN pore. In case of 13 Å pores, diffusivity coefficient increases significantly for both water and ethanol molecules. For 9 and 13 Å pores the water and ethanol molecules diffusion coefficients are higher than the pore size 7 Å, indicating more enhanced confinement effect at the lower pore size. Moreover, it is noted that there exist two and three density peaks of the oxygen atom of the water molecule and methyl and hydroxyl groups of the ethanol molecule inside the 9 and 13 Å pores, respectively. This indicates that the water and ethanol molecule diffuse rapidly in the larger slit pores (9 and 13 Å) compared to the narrow pore 7 Å. The results are agreement with recent works on ethanol/water transport through silicalite membranes[26] and alumina nanopores.[49] These results suggest that the diffusivities of ethanol and water molecules decrease with an increase in the ethanol concentration. This is attributed to the increase in ethanol binding with water with increasing ethanol concentration, as also observed by Zhao et al.[52] In addition, the diffusion coefficient for confined ethanol molecules is substantially less than that of water molecules inside various slit pores of graphene and hBN surfaces, which is akin to the behavior

observed in recent studies.[49,52] Furthermore, as expected, the diffusion coefficients of water and also ethanol molecules are obviously higher on the graphene compared to the hBN pores. In the graphene and hBN pores (7, 9, and 13 Å), the diffusion coefficient of ethanol and water molecules decreases with increases in ethanol content. These results clearly demonstrate that confined water and ethanol molecules mobility decreases at higher mole fraction of ethanol in mixtures.

We computed the residence time to estimate the average time that water and ethanol molecules remain within the pore, which is shown in Figure 9c,d. The time correlation function $C_R(t)$ is calculated using eq 4. Further, we calculated the residence time (τ_s) using time correlation function $C_R(t)$ using eq 5. The faster the autocorrelation function decays to 0, the shorter the residence time of water or ethanol molecules inside the pore. The time correction function for ethanol and water molecules inside the 7, 9, and 13 Å slit pores are shown in Figures S4 and S5 of the Supporting Information for different mole fractions of ethanol−water mixtures. The $C_R(t)$ decay rate is low and, thus, yield higher values of residence time (τ_s) of ethanol and water molecules. The results of $C_R(t)$ for water and ethanol molecules indicate that ethanol molecules reside inside the pore longer than water molecules for different compositions of ethanol in water. Comparing the residence time (τ_s) of water within graphene and hBN pores, it is apparent that water molecules reside inside the hBN pore longer than in the graphene pore. For example, for 0.3 mole fraction of ethanol, the residence times of water molecules within 7, 9, and 13 Å pores are 1200, 1150, and 1050 ps for hBN pore. In the case of graphene pore, the residence times of water molecules within 7, 9, and 13 Å are 1100, 1100, and 920 ps, respectively. We also observed that the residence time of water molecules decreases with increase in the pore widths (7, 9, and 13 Å). Water molecules confined between the graphene and hBN sheets within the slit-width of 7 Å reside longer as compared to those in 9 and 13 Å pores. The slow dynamical behavior of water in 7 Å pore size is supported by the structural properties of confined water molecules discussed in the earlier section. In the graphene and hBN pores (7, 9, and 13 Å), the water residence time in the mixtures increases with increasing ethanol content. These results clearly demonstrate that water mobility decreases at higher mole fraction of ethanol in ethanol−water mixtures.

The corresponding residence time results obtained for ethanol molecules are shown in Figure 9c,d. The $C_R(t)$ decays faster within the 9 and 13 Å pores than in the 7 Å for both graphene and hBN surface. The residence time of ethanol molecules substantially increases as the pore width decreases. This implies that ethanol molecules reside longer within the smaller pore size (7 Å) as compared to larger pore sizes (9 and 13 Å). Figure 9c,d shows higher residence time of confined water and ethanol molecules in the presence of hBN surface compared to the graphene surface. The residence time of the ethanol molecule inside the pores (7, 9, and 13 Å) of graphene and hBN surfaces increases with increasing mole fraction of ethanol. The result implies that the mobility of ethanol molecules decreases with the increase in mole fraction of ethanol in the mixture. This is probably related to the stronger effective attraction between ethanol molecules and hBN surface, which is clearly demonstrated in the later sections. The confined water and ethanol molecules have lower mobility and higher residence time within the pore 7 Å compared to the other pore sizes (9 and 13 Å). In 9 Å pore, the ethanol molecules show lower diffusion coefficient (0.15×10^{-9} m^2/

sec) value and higher residence time (1200 ps) on hBN surface compared to the graphene surface for 0.3 mole fraction of ethanol. Thus, adsorption amount of ethanol molecules within 9 Å pore of hBN pore should be higher compared to that in graphene pore, which is described more in detail in the next section.

3.4. Adsorption and Selectivity Analysis. Figure 10 shows the amount of ethanol and water molecules adsorbed per
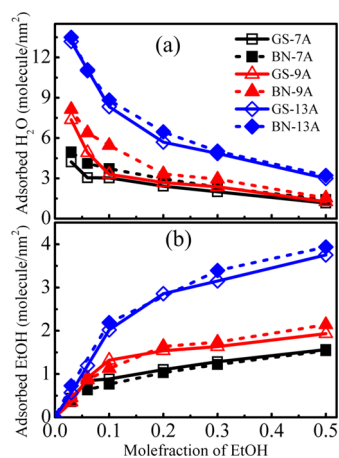
Figure 10. Adsorption of ethanol and water molecules within the pore as a function of mole fraction of ethanol. Filled symbols are for hBN and open symbols are for graphene.

unit surface area of the adsorbent in different pores as a function of mole fraction of ethanol. The amount of ethanol molecules increases with an increase in the width of the pore size, for both graphene and hBN pores. Furthermore, the amount of ethanol molecules increases with increasing mole fraction of ethanol. On the other hand, the adsorption of water within the slit pore decreases with increasing ethanol content inside the pore. At lower ethanol mole fraction, the number of ethanol molecules adsorbed within the pore is indifferent to the nature of the pore walls. However, at higher ethanol mole fraction, the number of ethanol molecules inside the hBN pore is higher compared to the graphene pore for different pore widths, which is more evident for bigger pore sizes. The adsorption of ethanol molecules on hBN pore is more than the graphene pore for all mole fractions of ethanol–water mixtures studied in this work. Within 13 Å pore width, the highest adsorption of ethanol molecules are found to be 3.6 and 4.0 molecule/nm², respectively, for graphene and hBN pores. Based on our simulations, the adsorption of ethanol molecules is higher in 13 Å pore compared to 9 and 7 Å pore for both walls (GS and hBN) for all mole fractions of ethanol–water mixtures. The difference in the adsorption behavior of ethanol and water molecules in graphene and hBN pores should affect the selectively of ethanol molecules over water molecules. Furthermore, the behavior is also an indication of pore size effect on the selectivity and separation process. A similar observation has been reported by Wang and co-workers[50] in their study on the molecular behavior of ethanol–water mixtures within variable size Au nanotubes.

Figure 11 presents the effect of pore width on the selectivity of ethanol over water for three different pores. The selectivity of ethanol at low mole fraction of ethanol is highest in hBN 9 Å pore. It is evident from the figure that the pore sizes 7 and 13 Å show lower selectivity of ethanol. In other words, the selectivity
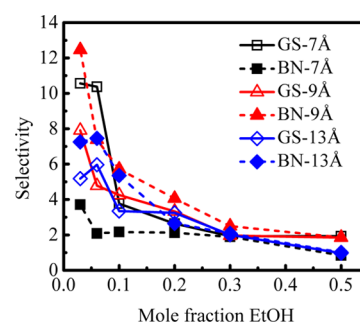
Figure 11. Selectivity of ethanol adsorption within three different graphene (GS) and hBN slit-shaped pores. Filled symbols are for hBN and open symbols are for graphene.

of the ethanol molecule within the 9 Å pore is higher compared to 7 and 13 Å pore sizes. When the pore size is small (7 Å), it can easily hold the smaller molecules like water, but hardly for the bigger ethanol molecules. Thus, water mainly enters the narrow slit pore of 7 Å, leading to a decrease in the selectivity of ethanol, which is well supported by the low values of ethanol adsorptions in slit pores for 7 Å pores (see Figure 11). For pore size, 9 Å, the relatively large number of ethanol molecules enters into the slit pore easily compared to the water molecules. Subsequently, the selectivity of an ethanol molecule is higher within 9 Å slit pore of hBN surface compared to the graphene surface. However, a further increase in the slit width to 13 Å decreases the selectivity of ethanol, as water is relatively more adsorbed (see Figure 11) compared to ethanol. Interestingly, the selectivity is slightly higher for the hBN pore compared to the graphene pore. This can be attributed to the relatively stronger ethanol–hBN interaction compared to water–hBN, which we present in detail in a later section using potential of mean force calculations. Based on the above results, it can be concluded that molecular sieving plays a more important role in lower pores, whereas surface–fluid interaction is a governing factor for larger pore sizes. In a recent work, Joshi et al.[77] using MD simulations have confirmed that the graphene-based materials with well-defined pore sizes can be used for filtration and separation technologies for the extraction of valuable solutes from complex mixtures. The graphene capillary acts as molecular sieves, blocking all solutes with hydrated radii larger than the capillary size. Our results show that the selectivity of ethanol decreases with an increase in mole fraction of ethanol. The selectivity of ethanol is higher for the 9 Å slit pore compared to 7 and 13 Å pores. The results confirm that the ethanol molecules easily permeate through the 9 Å slit pore compared to the 7 Å. Therefore, the pore width is the crucial parameter to dictate the selectivity of the ethanol. This suggests that pore 9 Å of hBN surface is promising for ethanol/water separation compared to the graphene surface. Therefore, this can be explained by using PMF profiles (see Figure S7 in the Supporting Information).

3.5. Potential of Mean Force Calculations. It is evident from the above results that preferentially adsorption capability for hBN is much more than that of graphene surface. To explore the underlying mechanism of the demonstrated adsorption and selectivity of ethanol and water molecules on graphene and hBN surfaces, we calculated the potential of mean force (PMF) based free energies for water and ethanol molecules. The separation of ethanol from water within pores is primarily due to the free-energy difference among the ethanol and water in pores. Thus, the PMF calculation would provide

an insight into the nature of water and ethanol within hBN and graphene pores. PMF method has been widely used as an effective tool in studying microscopic mechanism of various adsorption processes. For example, Sun et al.[78] explored the adsorption behavior of 13 different peptides on a hydrophobic surface using PMF. Kerisit et al.[79] studied the adsorption of solvent and impurity ions on a mineral surface using PMF. They observed that free energy profiles of metal ions, adsorbed on the surface, are correlated with solvent density. To this end, we calculate PMF as a function of distance between one molecule (water or ethanol) and the surface (graphene and hBN) using umbrella sampling.[80] A biasing potential is provided to the water or ethanol molecule, as shown in eq 11, to move the ethanol or water molecule from the bulk region to the solid surfaces (graphene or hBN).

$$w_i(\xi) = \frac{1}{2}K(\xi - \xi_i)^2 \tag{11}$$

where ξ is the distance between the center of mass of the molecule (water or ethanol) and solid surfaces (graphene or hBN), and ξ_i is the variation in the reaction coordinate from the solid surface. K is the initially applied umbrella potential used to provide a significant overlapping between windows. The biasing probability $\rho^{(b)}(\xi)$ of histogram data from MD simulation is post-processed using weighed histogram analysis method (WHAM),[81] as described in eqs 12 and 13. In the WHAM method, one uses an iterative process to determine the free energy constants, F_i. An initial guess set for F_i is used to estimate the unbiased probability $(\rho(\xi))$ distribution given by

$$\rho(\xi) = \frac{\sum_{i=1}^{Nw} n_i \rho_i^{(b)}(\xi)}{\sum_{j=1}^{Nw} n_j e^{-\beta(w_j(\xi) - F_j)}} \tag{12}$$

$$e^{-\beta F_i} = \int e^{-\beta w_i(\xi)} \rho(\xi) d\xi \tag{13}$$

The unbiased probability itself depends on the value of F_i; hence, the WHAM eqs 12 and 13 must be solved iteratively until they are self-consistent.

A representative PMF of ethanol and water adsorption as a function of distance from both surfaces (graphene and hBN) is shown in Figure 12a,b. The free energy profile shows an oscillating performance, when one ethanol molecule approaches to surfaces ($z = 0$ Å). As shown in Figure 12a, the PMF curves have three distinct minima located around 3.0, 6.5, and 9.2 Å, respectively, for both graphene and hBN surfaces. The first two deep minimum near the surface are usually referred to as the contact minimum (CM) between the ethanol molecule and surface (graphene and hBN) as well as the solvent layer-separated minimum (SLSM). A noticeably free energy barrier of adsorption appears at 6 Å from the graphene surface between CM and SLSM positions. The third minimum (TM) in the PMF curve is positioned at the bulk-interface transition region, where the ethanol molecule weakly interacts with the graphene surface. The free energy barrier of ethanol molecule in the interfacial region is obviously lower than the bulk phase, suggesting that the ethanol molecule has stronger tendency to approach the surface. In Figure 12a, two energy barriers are 0.34 and 1.5 kcal/mol, corresponding to the transfer of one ethanol molecule from the bulk to the graphene surface. Similarly, two energy barriers, 2.40 and 0.40 kcal/mol, are observed for the case of ethanol molecule transfer from the graphene surface to the bulk. In the case of hBN surface, two
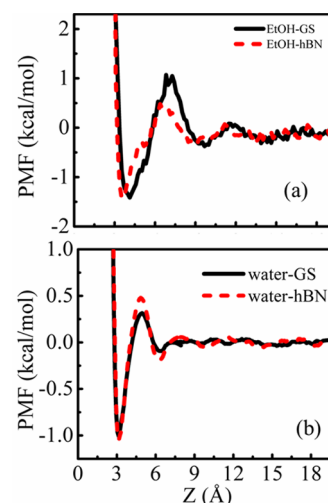
Figure 12. (a) Potential of mean force (PMF) as a function of distance between the one ethanol molecule and graphene (GS) and hBN surfaces. (b) Potential of mean force (PMF) as a function of distance between the one water molecule and graphene (GS) and hBN surfaces.

energy barriers are 0.37 and 1.00 kcal/mol, for one ethanol molecule transfer from the bulk to the hBN surface. The corresponding energy barriers for the reverse process, ethanol molecule transfer from the hBN surface to the bulk, are 2.00 and 0.40 kcal/mol. Each free energy barrier represents a separated adsorption/desorption process step. The lower energy barrier represents the ethanol molecule can easily adsorb on the hBN surface. This suggests that the ethanol is preferentially adsorbed on hBN surface compared to graphene surface.

In the Figure 12b, we report the PMF profiles of one water molecule on both graphene and hBN surfaces. There is a significant difference in the PMF profiles of water molecules obtained from graphene and hBN surfaces. The three distinct minima are located around at 3.0, 6.0, and 9.0 Å from both the surface. For graphene surface, the water molecule faces two energy barriers, namely, 0.1 and 0.40 kcal/mol, respectively, during the transfer from the bulk to the surface. The corresponding energy barriers for the case of hBN surface are 0.15 and 0.70 kcal/mol. The two energy barriers for the transfer of water molecule from surface to bulk are 1.25 and 0.2 kcal/mol, for the graphene surface, and 1.5 and 0.3 kcal/mol for the hBN surface. The free energy barrier is lower for the water molecules to adsorb on graphene and hBN surfaces. Thus, it is clear that once adsorbed, the adsorbed water molecules on hBN/graphene surface can easily desorb from the surface compared to the ethanol molecules.

4. CONCLUSIONS

In summary, we have employed molecular dynamics simulations to investigate the adsorption of ethanol from ethanol–water mixtures using the slit shaped graphene and hBN pores of different widths. The investigation of the structural properties of the confined ethanol and water molecules within different pore widths are used to elucidate the adsorption behavior. Results from this study showed that the adsorption of ethanol molecules inside the hBN and graphene pore increases with the increasing mole fraction of ethanol–water mixture. The hBN pores have demonstrated higher selectivity for the ethanol–

water mixtures compared to the graphene pores. By comparing the selectivity of ethanol molecules within the different slit pores, 9 Å slit pore shows the highest efficiency of ethanol–water separation compared to the 7 and 13 Å pores. The combination of structural and dynamical properties results reported here for ethanol–water system suggests that pore size 9 Å of hBN surface are useful for the separation of ethanol from ethanol–water system. This behavior is well supported by the potential of mean force calculation which clearly suggests lower free-energy value for ethanol in hBN pores.

■ ASSOCIATED CONTENT

Ⓢ Supporting Information

The Supporting Information is available free of charge on the ACS Publications website at DOI: 10.1021/acs.jpcc.7b00172.

> The snapshots of water and ethanol molecules within the 7, 9, and 13 Å graphene and hBN slit pores. The residence autocorrelation function, mean square displacement, and potential mean force of water and ethanol molecules within the 7, 9, and 13 Å graphene and hBN slit-shaped pores (PDF).

■ AUTHOR INFORMATION

Corresponding Author

*E-mail: jayantks@iitk.ac.in. Tel.: 91-512-259 6141. Fax: 91-512-259 0104.

ORCID Ⓘ

Jayant K. Singh: 0000-0001-8056-2115

Notes

The authors declare no competing financial interest.

■ ACKNOWLEDGMENTS

■ REFERENCES

(1) Shannon, M. A.; Bohn, P. W.; Elimelech, M.; Georgiadis, J. G.; Marinas, B. J.; Mayes, A. M. Science and Technology for Water Purification in the Coming Decades. *Nature* **2008**, *452*, 301−310.

(2) Montgomery, M. A.; Elimelech, M. Water and Sanitation in Developing Countries: Including Health in the Equation. *Environ. Sci. Technol.* **2007**, *41*, 17−24.

(3) Zhang, F.; Zhang, W. B.; Shi, Z.; Wang, D.; Jin, J.; Jiang, L. Nanowire-Haired Inorganic Membranes with Superhydrophilicity and Underwater Ultralow Adhesive Superoleophobicity for High-Efficiency Oil/Water Separation. *Adv. Mater.* **2013**, *25*, 4192−4198.

(4) Alyüz, B.; Veli, S. Kinetics and Equilibrium Studies for the Removal of Nickel and Zinc from Aqueous Solutions by Ion Exchange Resins. *J. Hazard. Mater.* **2009**, *167*, 482−488.

(5) El Samrani, A. G.; Lartiges, B. S.; Villiéras, F. Chemical Coagulation of Combined Sewer Overflow: Heavy Metal Removal and Treatment Optimization. *Water Res.* **2008**, *42*, 951−960.

(6) Ghosh, P.; Samanta, A. N.; Ray, S. Reduction of Cod and Removal of Zn^{2+} from Rayon Industry Wastewater by Combined Electro-Fenton Treatment and Chemical Precipitation. *Desalination* **2011**, *266*, 213−217.

(7) Cséfalvay, E.; Pauer, V.; Mizsey, P. Recovery of Copper from Process Waters by Nanofiltration and Reverse Osmosis. *Desalination* **2009**, *240*, 132−142.

(8) Yanagisawa, H.; Matsumoto, Y.; Machida, M. Adsorption of Zn(II) and Cd(II) Ions onto Magnesium and Activated Carbon Composite in Aqueous Solution. *Appl. Surf. Sci.* **2010**, *256*, 1619−1623.

(9) Alidokht, L.; Khataee, A. R.; Reyhanitabar, A.; Oustan, S. Cr(VI) Immobilization Process in a Cr-Spiked Soil by Zerovalent Iron Nanoparticles: Optimization Using Response Surface Methodology. *Clean: Soil, Air, Water* **2011**, *39*, 633−640.

(10) Khataee, A. R.; Kasiri, M. B.; Alidokht, L. Application of Response Surface Methodology in the Optimization of Photocatalytic Removal of Environmental Pollutants Using Nanocatalysts. *Environ. Technol.* **2011**, *32*, 1669−1684.

(11) Bayat, A.; Aghamiri, S. F.; Moheb, A.; Vakili-Nezhaad, G. R. Oil Spill Cleanup from Sea Water by Sorbent Materials. *Chem. Eng. Technol.* **2005**, *28*, 1525−1528.

(12) Adebajo, M. O.; Frost, R. L.; Kloprogge, J. T.; Carmody, O.; Kokot, S. Porous Materials for Oil Spill Cleanup: A Review of Synthesis and Absorbing Properties. *J. Porous Mater.* **2003**, *10*, 159−170.

(13) Deschamps, G.; Caruel, H.; Borredon, M.-E.; Bonnin, C.; Vignoles, C. Oil Removal from Water by Selective Sorption on Hydrophobic Cotton Fibers. 1. Study of Sorption Properties and Comparison with Other Cotton Fiber-Based Sorbents. *Environ. Sci. Technol.* **2003**, *37*, 1013−1015.

(14) Sohn, K.; Joo, N. Y.; Chang, H.; Roh, K.-M.; Dong Jang, H.; Huang, J. Oil Absorbing Graphene Capsules by Capillary Molding. *Chem. Commun.* **2012**, *48*, 5968−5970.

(15) Thanikaivelan, P.; Narayanan, N. T.; Pradhan, B. K.; Ajayan, P. M. Collagen Based Magnetic Nanocomposites for Oil Removal Applications. *Sci. Rep.* **2012**, *2*, 230.

(16) Zhu, Q.; Pan, Q.; Liu, F. Facile Removal and Collection of Oils from Water Surfaces through Superhydrophobic and Superoleophilic Sponges. *J. Phys. Chem. C* **2011**, *115*, 17464−17470.

(17) Calcagnile, P.; Fragouli, D.; Bayer, I. S.; Anyfantis, G. C.; Martiradonna, L.; Cozzoli, P. D.; Cingolani, R.; Athanassiou, A. Magnetically Driven Floating Foams for the Removal of Oil Contaminants from Water. *ACS Nano* **2012**, *6*, 5413−5419.

(18) Yuan, J.; Liu, X.; Akbulut, O.; Hu, J.; Suib, S. L.; Kong, J.; Stellacci, F. Superwetting Nanowire Membranes for Selective Absorption. *Nat. Nanotechnol.* **2008**, *3*, 332−336.

(19) Cong, H.-P.; Ren, X.-C.; Wang, P.; Yu, S.-H. Macroscopic Multifunctional Graphene-Based Hydrogels and Aerogels by a Metal Ion Induced Self-Assembly Process. *ACS Nano* **2012**, *6*, 2693−2703.

(20) Bondy, S. C.; Guo, S. X. Effect of Ethanol Treatment on Indices of Cumulative Oxidative Stress. *Eur. J. Pharmacol., Environ. Toxicol. Pharmacol. Sect.* **1994**, *270*, 349−355.

(21) Faisal, M.; Khan, S. B.; Rahman, M. M.; Jamal, A.; Umar, A. Ethanol Chemi-Sensor: Evaluation of Structural, Optical and Sensing Properties of CuO Nanosheets. *Mater. Lett.* **2011**, *65*, 1400−1403.

(22) Zhang, K.; Lively, R. P.; Noel, J. D.; Dose, M. E.; McCool, B. A.; Chance, R. R.; Koros, W. J. Adsorption of Water and Ethanol in MFI-Type Zeolites. *Langmuir* **2012**, *28*, 8664−8673.

(23) Simo, M.; Sivashanmugam, S.; Brown, C. J.; Hlavacek, V. Adsorption/Desorption of Water and Ethanol on 3A Zeolite in near-Adiabatic Fixed Bed. *Ind. Eng. Chem. Res.* **2009**, *48*, 9247−9260.

(24) Ahmed, I.; Pa, N. F. C.; Nawawi, M. G. M.; Rahman, W. A. W. A. Modified Polydimethylsiloxane/Polystyrene Blended IPN Pervaporation Membrane for Ethanol/Water Separation. *J. Appl. Polym. Sci.* **2011**, *122*, 2666−2679.

(25) Lai, C.-L.; Liou, R.-M.; Chen, S.-H.; Shih, C.-Y.; Chang, J. S.; Huang, C.-H.; Hung, M.-Y.; Lee, K.-R. Dehydration of Ethanol/Water Mixture by Asymmetric Ion-Exchange Membranes. *Desalination* **2011**, *266*, 17−24.

(26) Yang, J. Z.; Liu, Q. L.; Wang, H. T. Analyzing Adsorption and Diffusion Behaviors of Ethanol/Water through Silicalite Membranes by Molecular Simulation. *J. Membr. Sci.* **2007**, *291*, 1−9.

(27) Sano, T.; Yanagishita, H.; Kiyozumi, Y.; Mizukami, F.; Haraya, K. Separation of Ethanol/Water Mixture by Silicalite Membrane on Pervaporation. *J. Membr. Sci.* **1994**, *95*, 221−228.

(28) Zhang, J.; Liu, W. Thin Porous Metal Sheet-Supported NaA Zeolite Membrane for Water/Ethanol Separation. *J. Membr. Sci.* **2011**, *371*, 197−210.

(29) Vane, L. M.; Namboodiri, V. V.; Bowen, T. C. Hydrophobic Zeolite-Silicone Rubber Mixed Matrix Membranes for Ethanol-Water Separation: Effect of Zeolite and Silicone Component Selection on Pervaporation Performance. *J. Membr. Sci.* **2008**, *308*, 230−241.

(30) Chen, S.-H.; Yu, K.-C.; Lin, S.-S.; Chang, D.-J.; Liou, R. M. Pervaporation Separation of Water/Ethanol Mixture by Sulfonated Polysulfone Membrane. *J. Membr. Sci.* **2001**, *183*, 29−36.

(31) Nguyen, Q. T.; Le Blanc, L.; Neel, J. Preparation of Membranes from Polyacrylonitrile-Polyvinylpyrrolidone Blends and the Study of Their Behaviour in the Pervaporation of Water-Organic Liquid Mixtures. *J. Membr. Sci.* **1985**, *22*, 245−255.

(32) Lin, Y.; Connell, J. W. Advances in 2D Boron Nitride Nanostructures: Nanosheets, Nanoribbons, Nanomeshes, and Hybrids with Graphene. *Nanoscale* **2012**, *4*, 6908−6939.

(33) Terrones, M.; et al. Graphene and Graphite Nanoribbons: Morphology, Properties, Synthesis, Defects and Applications. *Nano Today* **2010**, *5*, 351−372.

(34) Iijima, S. Helical Microtubules of Graphitic Carbon. *Nature* **1991**, *354*, 56−58.

(35) Zeng, H.; Zhi, C.; Zhang, Z.; Wei, X.; Wang, X.; Guo, W.; Bando, Y.; Golberg, D. ″White Graphenes″: Boron Nitride Nanoribbons Via Boron Nitride Nanotube Unwrapping. *Nano Lett.* **2010**, *10*, 5049−5055.

(36) Song, L.; et al. Large Scale Growth and Characterization of Atomic Hexagonal Boron Nitride Layers. *Nano Lett.* **2010**, *10*, 3209−3215.

(37) Ooi, N.; Rairkar, A.; Lindsley, L.; Adams, J. B. Electronic Structure and Bonding in Hexagonal Boron Nitride. *J. Phys.: Condens. Matter* **2006**, *18*, 97.

(38) Pacilé, D.; Meyer, J. C.; Girit, Ç. Ö.; Zettl, A. The Two-Dimensional Phase of Boron Nitride: Few-Atomic-Layer Sheets and Suspended Membranes. *Appl. Phys. Lett.* **2008**, *92*, 133107.

(39) Ribeiro, R. M.; Peres, N. M. R. Stability of Boron Nitride Bilayers: Ground-State Energies, Interlayer Distances, and Tight-Binding Description. *Phys. Rev. B: Condens. Matter Mater. Phys.* **2011**, *83*, 235312.

(40) Lee, C.; Li, Q.; Kalb, W.; Liu, X.-Z.; Berger, H.; Carpick, R. W.; Hone, J. Frictional Characteristics of Atomically Thin Sheets. *Science* **2010**, *328*, 76−80.

(41) Severin, N.; Sokolov, I. M.; Rabe, J. P. Dynamics of Ethanol and Water Mixtures Observed in a Self-Adjusting Molecularly Thin Slit Pore. *Langmuir* **2014**, *30*, 3455−3459.

(42) Lei, W.; Portehault, D.; Liu, D.; Qin, S.; Chen, Y. Porous Boron Nitride Nanosheets for Effective Water Cleaning. *Nat. Commun.* **2013**, *4*, 1777.

(43) Li, J.; Xiao, X.; Xu, X.; Lin, J.; Huang, Y.; Xue, Y.; Jin, P.; Zou, J.; Tang, C. Activated Boron Nitride as an Effective Adsorbent for Metal Ions and Organic Pollutants. *Sci. Rep.* **2013**, *3*, 3208.

(44) Liu, F.; Yu, J.; Ji, X.; Qian, M. Nanosheet-Structured Boron Nitride Spheres with a Versatile Adsorption Capacity for Water Cleaning. *ACS Appl. Mater. Interfaces* **2015**, *7*, 1824−1832.

(45) Tian, X.; Yang, Z.; Zhou, B.; Xiu, P.; Tu, Y. Alcohol-Induced Drying of Carbon Nanotubes and Its Implications for Alcohol/Water Separation: A Molecular Dynamics Study. *J. Chem. Phys.* **2013**, *138*, 204711.

(46) Wakisaka, A.; Matsuura, K.; Uranaga, M.; Sekimoto, T.; Takahashi, M. Azeotropy of Alcohol-Water Mixtures from the Viewpoint of Cluster-Level Structures. *J. Mol. Liq.* **2011**, *160*, 103−108.

(47) Wakisaka, A.; Komatsu, S.; Usui, Y. Solute-Solvent and Solvent-Solvent Interactions Evaluated through Clusters Isolated from Solutions: Preferential Solvation in Water-Alcohol Mixtures. *J. Mol. Liq.* **2001**, *90*, 175−184.

(48) Onori, G. Adiabatic Compressibility and Structure of Aqueous Solutions of Ethyl Alcohol. *J. Chem. Phys.* **1988**, *89*, 4325−4332.

(49) Phan, A.; Cole, D. R.; Striolo, A. Preferential Adsorption from Liquid Water-Ethanol Mixtures in Alumina Pores. *Langmuir* **2014**, *30*, 8066−8077.

(50) Wang, Y.-C.; Ju, S.-P.; Lee, W.-J.; Chen, H.-T.; Hsieh, J.-Y. Effect of Au Nanotube Size on Molecular Behavior of Water/Ethanol Mixtures. *RSC Adv.* **2013**, *3*, 5860−5870.

(51) Guo, X.-Y.; Watermann, T.; Sebastiani, D. Local Microphase Separation of a Binary Liquid under Nanoscale Confinement. *J. Phys. Chem. B* **2014**, *118*, 10207−10213.

(52) Zhao, M.; Yang, X. Segregation Structures and Miscellaneous Diffusions for Ethanol/Water Mixtures in Graphene-Based Nanoscale Pores. *J. Phys. Chem. C* **2015**, *119*, 21664−21673.

(53) Jorgensen, W. L.; Maxwell, D. S.; Tirado-Rives, J. Development and Testing of the OPLS All-Atom Force Field on Conformational Energetics and Properties of Organic Liquids. *J. Am. Chem. Soc.* **1996**, *118*, 11225−11236.

(54) Argyris, D.; Tummala, N. R.; Striolo, A.; Cole, D. R. Molecular Structure and Dynamics in Thin Water Films at the Silica and Graphite Surfaces. *J. Phys. Chem. C* **2008**, *112*, 13587−13599.

(55) Dutta, R. C.; Khan, S.; Singh, J. K. Wetting Transition of Water on Graphite and Boron-Nitride Surfaces: A Molecular Dynamics Study. *Fluid Phase Equilib.* **2011**, *302*, 310−315.

(56) Metya, A. K.; Khan, S.; Singh, J. K. Wetting Transition of the Ethanol-Water Droplet on Smooth and Textured Surfaces. *J. Phys. Chem. C* **2014**, *118*, 4113−4121.

(57) Berendsen, H. J. C.; Grigera, J. R.; Straatsma, T. P. The Missing Term in Effective Pair Potentials. *J. Phys. Chem.* **1987**, *91*, 6269−6271.

(58) Liu, P.; Harder, E.; Berne, B. J. On the Calculation of Diffusion Coefficients in Confined Fluids and Interfaces with an Application to the Liquid-Vapor Interface of Water. *J. Phys. Chem. B* **2004**, *108*, 6595−6602.

(59) Sircar, S.; Novosad, J.; Myers, A. L. Adsorption from Liquid Mixtures on Solids: Thermodynamics of Excess Properties and Their Temperature Coefficients. *Ind. Eng. Chem. Fundam.* **1972**, *11*, 249−254.

(60) Luzar, A.; Chandler, D. Hydrogen-Bond Kinetics in Liquid Water. *Nature* **1996**, *379*, 55−57.

(61) Chandra, A. Effects of Ion Atmosphere on Hydrogen-Bond Dynamics in Aqueous Electrolyte Solutions. *Phys. Rev. Lett.* **2000**, *85*, 768−771.

(62) Saiz, L.; Padró, J. A.; Guàrdia, E. Structure and Dynamics of Liquid Ethanol. *J. Phys. Chem. B* **1997**, *101*, 78−86.

(63) Plimpton, S. Fast Parallel Algorithms for Short-Range Molecular Dynamics. *J. Comput. Phys.* **1995**, *117*, 1−19.

(64) Allen, M. P.; Tildesley, D. J. *Computer Simulation of Liquids*; Oxford University Press: Oxford, 2004.

(65) Ryckaert, J.-P.; Ciccotti, G.; Berendsen, H. J. C. Numerical Integration of the Cartesian Equations of Motion of a System with Constraints: Molecular Dynamics of N-Alkanes. *J. Comput. Phys.* **1977**, *23*, 327−341.

(66) Nosé, S. A Unified Formulation of the Constant Temperature Molecular Dynamics Methods. *J. Chem. Phys.* **1984**, *81*, 511−519.

(67) Hirunsit, P.; Balbuena, P. B. Effects of Confinement on Water Structure and Dynamics: A Molecular Simulation Study. *J. Phys. Chem. C* **2007**, *111*, 1709−1715.

(68) Mosaddeghi, H.; Alavi, S.; Kowsari, M. H.; Najafi, B. Simulations of Structural and Dynamic Anisotropy in Nano-Confined Water between Parallel Graphite Plates. *J. Chem. Phys.* **2012**, *137*, 184703.

(69) Jedlovszky, P.; Vincze, A.; Horvai, G. New Insight into the Orientational Order of Water Molecules at the Water/1,2-Dichloroethane Interface: A Monte Carlo Simulation Study. *J. Chem. Phys.* **2002**, *117*, 2271−2280.

(70) Jedlovszky, P.; Vincze, A.; Horvai, G. Full Description of the Orientational Statistics of Molecules near to Interfaces. Water at the Interface with CCl$_4$. *Phys. Chem. Chem. Phys.* **2004**, *6*, 1874−1879.

(71) Lívia, P.; Pál, J.; Horvai, G. Structure of the Acetone Liquid-Vapor Interface as Seen from Monte Carlo Simulations. *J. Phys. Chem. B* **2005**, *109*, 12014−12019.

(72) Iiyama, T.; Hagi, K.; Urushibara, T.; Ozeki, S. Direct Determination of Intermolecular Structure of Ethanol Adsorbed in Micropores Using X-Ray Diffraction and Reverse Monte Carlo Analysis. *Colloids Surf., A* **2009**, *347*, 133−141.

(73) Ohkubo, T.; Iiyama, T.; Nishikawa, K.; Suzuki, T.; Kaneko, K. Pore-Width-Dependent Ordering of C_2H_5OH Molecules Confined in Graphitic Slit Nanospaces. *J. Phys. Chem. B* **1999**, *103*, 1859−1863.

(74) Ohkubo, T.; Kaneko, K. Oriented Structures of Alcohol Hidden in Carbon Micropores with ERDF Analysis. *Colloids Surf., A* **2001**, *187*, 177−185.

(75) Ye, H.; Zhang, H.; Zheng, Y.; Zhang, Z. Nanoconfinement Induced Anomalous Water Diffusion inside Carbon Nanotubes. *Microfluid. Nanofluid.* **2011**, *10*, 1359−1364.

(76) Zheng, Y.-g.; Ye, H.-f.; Zhang, Z.-q.; Zhang, H.-w. Water Diffusion inside Carbon Nanotubes: Mutual Effects of Surface and Confinement. *Phys. Chem. Chem. Phys.* **2012**, *14*, 964−971.

(77) Joshi, R. K.; Carbone, P.; Wang, F. C.; Kravets, V. G.; Su, Y.; Grigorieva, I. V.; Wu, H. A.; Geim, A. K.; Nair, R. R. Precise and Ultrafast Molecular Sieving through Graphene Oxide Membranes. *Science* **2014**, *343*, 752.

(78) Sun, Y.; Dominy, B. N.; Latour, R. A. Comparison of Solvation-Effect Methods for the Simulation of Peptide Interactions with a Hydrophobic Surface. *J. Comput. Chem.* **2007**, *28*, 1883−1892.

(79) Kerisit, S.; Parker, S. C. Free Energy of Adsorption of Water and Metal Ions on the {1014} Calcite Surface. *J. Am. Chem. Soc.* **2004**, *126*, 10152−10161.

(80) Roux, B. The Calculation of the Potential of Mean Force Using Computer Simulations. *Comput. Phys. Commun.* **1995**, *91*, 275−282.

(81) Souaille, M.; Roux, B. Extension to the Weighted Histogram Analysis Method: Combining Umbrella Sampling with Free Energy Calculations. *Comput. Phys. Commun.* **2001**, *135*, 40−57.